

# High-performance polyaniline-coated electrospun P(VDF-TrFE)/BaTiO<sub>3</sub> nanofiber-based flexible piezoelectric nanogenerator

Biswajit Mahanty<sup>a</sup>, Sujoy Kumar Ghosh<sup>b</sup>, Dong-Weon Lee<sup>a,c,d,\*</sup>

<sup>a</sup> MEMS and Nanotechnology Laboratory, School of Mechanical Engineering, Chonnam National University, Gwangju, 61186, Republic of Korea

<sup>b</sup> Department of Condensed Matter Physics and Material Sciences, S.N. Bose National Centre for Basic Sciences, Block JD, Sector III, Salt Lake, Kolkata, 700106, India

<sup>c</sup> Advanced Medical Device Research Center for Cardiovascular Disease, Chonnam National University, 77 Yongbong-ro, Buk-gu, Gwangju, 61186, Republic of Korea

<sup>d</sup> Center for Next-Generation Sensor Research and Development, Chonnam National University, Gwangju, 61186, Republic of Korea

## ARTICLE INFO

### Keywords:

Polyaniline-coated nanocomposite nanofibers  
Ferroelectric barium titanate  
poly(vinylidene fluoride-co-trifluoroethylene)  
Composite nanofibers  
Piezoelectric nanogenerators

## ABSTRACT

The rapid progress and assimilation of the Internet of Things in modern lifestyles has sparked increased interest in self-powered electronics and wearable sensors. In this study, we present a simple, facile, and cost-effective approach to fabricate polyaniline (PANI)-coated poly(vinylidene fluoride-co-trifluoroethylene) (P(VDF-TrFE))/barium titanate (BT) nanocomposite nanofiber mats. The addition of PANI-coated BT NPs into the nanofibers greatly enhances the piezoelectric coefficient ( $d_{33} \approx 62 \text{ pC N}^{-1}$ ), leading to an improved output voltage. Meanwhile, the conductive PANI also improves the electrically conductive network, resulting in enhanced current output. The proposed flexible piezoelectric nanogenerator yielded an excellent figure of merit ( $14.4 \times 10^{-11} \text{ Pa}^{-1}$ ), significantly enhancing energy-harvesting performance (an open-circuit output voltage of  $\sim 68 \text{ V}$ , a short-circuit current of  $\sim 3 \text{ }\mu\text{A}$ , and a remarkable power density of  $225 \text{ mW m}^{-2}$ ). Furthermore, the fabricated flexible devices exhibited an average mechano-sensitivity of  $1.2 \text{ V kPa}^{-1}$ , showcasing its potential for widespread application in self-powered wearable sensors capable of capturing various human motions in applications such as gesture monitoring and finger motion detection.

## 1. Introduction

By harnessing energy from environmental and biomechanical vibrations, nanogenerators can eliminate the need for traditional power sources such as batteries and prove useful as supplementary power sources for low-power electronic devices, ranging from consumer electronics to healthcare [1], implantable devices [2], environmental monitoring [3], wearable sensor networks [4], and beyond. Despite the high performance of triboelectric nanogenerators (TENGs), in recent years, piezoelectric nanogenerators (PENGs) have continued to be successful in satisfying industrial requirements and attracting greater interest toward commercialization [5]. However, there are still challenges to overcome, such as enhancing the power output performance, efficiency, reducing cost, and integrating the technology seamlessly into existing products and systems. Several materials are useful in overcoming the performance difficulties. Piezoelectric ceramics are commonly utilized in energy-harvesting devices owing to their remarkable piezoelectric properties. However, the inherent brittleness

of these materials imposes significant constraints on their practical implementation in wearable electronics and healthcare-monitoring systems, where flexibility and mechanical resilience are of paramount importance [6–8]. In recent years, polymer-based piezoelectric materials such as poly(vinylidene fluoride) (PVDF) and its copolymers poly(vinylidene fluoride-co-trifluoroethylene) (P(VDF-TrFE)) have gained importance in wearable applications because of their exceptional mechanical flexibility, ease of fabrication, environment friendliness, and biocompatibility [9–13]. Among different VDF molar content in P(VDF-TrFE) copolymers, 70 mol% VDF content-based P(VDF-TrFE) polymer shown largest transverse piezoelectricity and higher piezoelectric power generation capability which is ideally suitable energy harvesting applications [14]. The presence of the electroactive  $\beta$ -phase in these polymer materials leads to spontaneous polarization of dipoles, resulting in piezoelectric behavior [15]. However, a low electroactive  $\beta$ -phase content in P(VDF-TrFE) can lead to reduced piezoelectric response and sensitivity to mechanical deformation. To date, various techniques have been proposed to enhance the electroactive  $\beta$ -phase

\* Corresponding author. MEMS and Nanotechnology Laboratory, School of Mechanical Engineering, Chonnam National University, Gwangju, 61186, Republic of Korea.

E-mail address: [mems@jnu.ac.kr](mailto:mems@jnu.ac.kr) (D.-W. Lee).

<https://doi.org/10.1016/j.mtnano.2023.100421>

Received 3 August 2023; Received in revised form 25 September 2023; Accepted 8 October 2023

Available online 14 October 2023

2588-8420/© 2023 Published by Elsevier Ltd.

content including (but not limited to) mechanical stretching [16], electrical poling [17], solution casting [18], filler incorporation [19], spin coating [20], and electrospinning [21]. Among them, the in situ electrical poling process during electrospinning and the enhancement of the  $\beta$ -phase through the incorporation of high-piezoelectric-coefficient materials (such as barium titanate (BT) [22]) or conductive polymer-based fillers (such as polyaniline (PANI) [23], which is one of the most promising conductive filler materials and is extensively used for energy-storage devices because of its low cost, easy synthesis process, and controllable electrical conductivity in the P(VDF-TrFE) matrix have been shown to significantly improve the piezoelectric performance of PENGs. To further improve device performances, in addition to single-filler doping, for better results, researchers have explored double-filler doping to realize a synergistic effect of improving the  $\beta$ -phase content and excellent electrical conductivity to promote charge transfer. Some examples include dual piezoelectric materials, the addition of BaTiO<sub>3</sub> and ZnO nanorods in PVDF (PVDF/BaTiO<sub>3</sub>/ZnO composite nanofiber) ( $V_{oc} \approx 12$  V) [24], electrospun PVDF/KNN/ZnO nanocomposite nanofiber ( $V_{oc} \approx 25$  V,  $I_{sc} \approx 1.81$   $\mu$ A) [25], piezoelectric materials and conductive materials such as PVDF/KNN/CNT composite nanofiber films ( $V_{oc} \approx 23.24$  V,  $I_{sc} \approx 9$   $\mu$ A) [26], PVDF/graphene-ZnO nanocomposite nanofiber film ( $V_{oc} \approx 840$  mV) [27], and PVDF/graphene/BaTiO<sub>3</sub> composite nanofiber films ( $V_{oc} \approx 11$  V and power  $\approx 4.1$   $\mu$ W) [28]. However, the reported output power from the nanofiber-based PENGs to date has only been in the range of a few microwatts owing to the limited improvement in piezoelectric coefficients ( $d_{33}$ ) in the range of 3.9–44 pC N<sup>-1</sup> (Table S1).

In this study, we adopt a comprehensive and facile approach to fabricate a PANI-coated P(VDF-TrFE)/BT (PANI@P(VDF-TrFE)/BT) nanocomposite nanofiber-based flexible piezoelectric nanogenerator (PA-PENG) for human motion detection. The fabricated PA-PENG generated a voltage output of 68 V, current output of 3  $\mu$ A, and power output of 225 mW m<sup>-2</sup>. BT NPs effectively improve the piezoelectric coefficients through interfacial interactions with the P(VDF-TrFE) chains, while conductive PANI mainly facilitates the charge transport along with the improvement of the electroactive  $\beta$ -phase. Because of its

excellent sensitivity, the PA-PENG can be effectively utilized as a portable power source, biomechanical energy harvester, physiological signal monitoring.

## 2. Results and discussion

### 2.1. Degree of crystallinity and $\beta$ -phase content improvement

The solution preparation process and methodologies employed for synthesizing P(VDF-TrFE) nanofibers, BT NP-incorporated P(VDF-TrFE) (P(VDF-TrFE)/BT), and PANI-coated P(VDF-TrFE)/BT (PANI@P(VDF-TrFE)/BT) nanocomposite nanofibers are schematically illustrated in Fig. 1 and described in detail in the experimental section. It is important to note that in certain crystalline materials, such as polyvinylidene fluoride (PVDF) and its copolymers, the presence of a higher  $\beta$ -phase content and an increased degree of crystallinity tends to promote a stronger dipolar orientation within the material's molecular structure. Because of this enhanced dipolar alignment, the piezoelectric properties of these materials are also augmented [29]. The effect of incorporation of BT NPs (10 wt%) into pure P(VDF-TrFE) nanofibers before and after PANI coating in the form of  $\beta$ -phase and crystallinity content was investigated through FT-IR spectra and XRD analyses (Fig. 2a–c). The FT-IR spectra (Fig. 2a) revealed that the pure P(VDF-TrFE) nanofibers and composite nanofibers showed vibrational bands at 841 and 1286 cm<sup>-1</sup>, which were attributed to the piezoelectric  $\beta$ -crystalline phase [10]. There is no existence of  $\alpha$ -phase found in the pure P(VDF-TrFE) and its nanocomposite nanofibers (Fig. 2a). Furthermore, all the  $\beta$ -crystalline phase peaks at 841, 1286, and 1400 cm<sup>-1</sup> are attributing to the CF<sub>2</sub> symmetric stretching, CF<sub>2</sub> symmetric stretching, and CH<sub>2</sub> wagging vibration, respectively, for pure P(VDF-TrFE) and its nanocomposite nanofibers [30]. The formation of the piezoelectric  $\beta$ -crystalline phase in the pure P(VDF-TrFE) nanofibers could be attributed to the simultaneous poling and stretching during the electrospinning process [31]. Besides this, the characteristic vibrational bands observed at 1583 and 1493 cm<sup>-1</sup>, in PANI@P(VDF-TrFE)/BT composite nanofibers, are mainly attributed to the stretching modes of C=C originating from

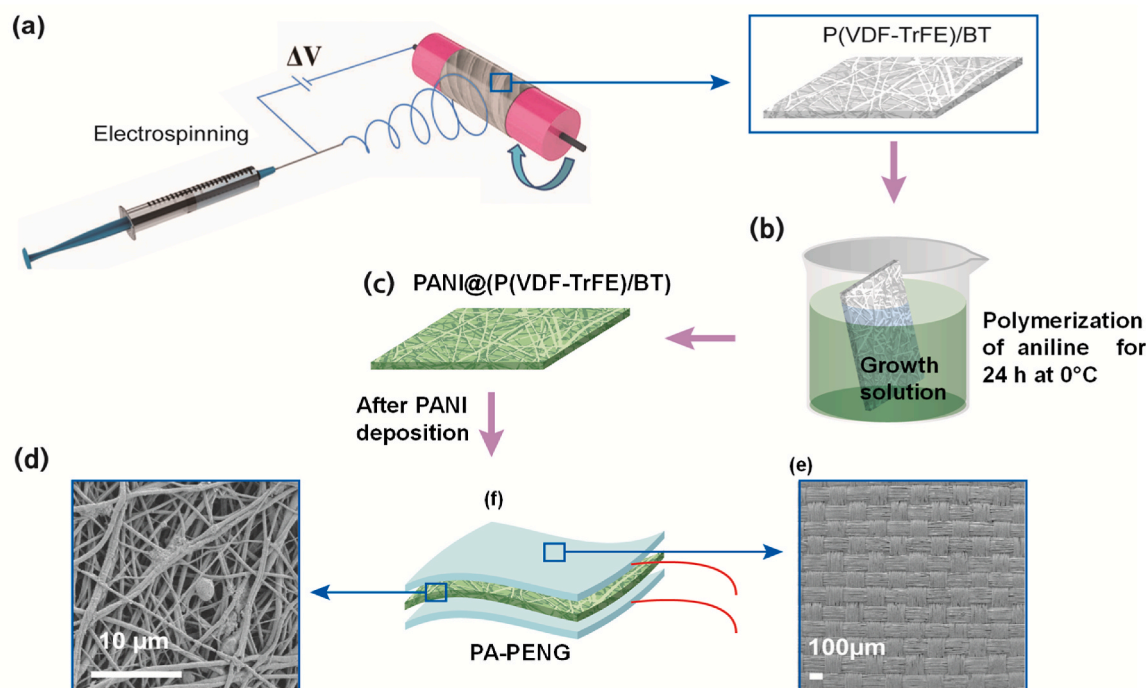


**Fig. 1.** Schematic diagram illustrating the deposition and designing process of PANI on P(VDF-TrFE)/BT nanocomposite nanofibers and PA-PENG device, respectively. (a) Electrospinning process, (b) polymerization of aniline for 24 h at 0 °C, and (c) P(VDF-TrFE)/BT nanocomposite nanofibers after PANI deposition. FE-SEM images of (d) PANI@P(VDF-TrFE)/BT nanocomposite nanofibers and (e) Cu-Ni polyester microfabric electrode, and (f) design of PA-PENG.

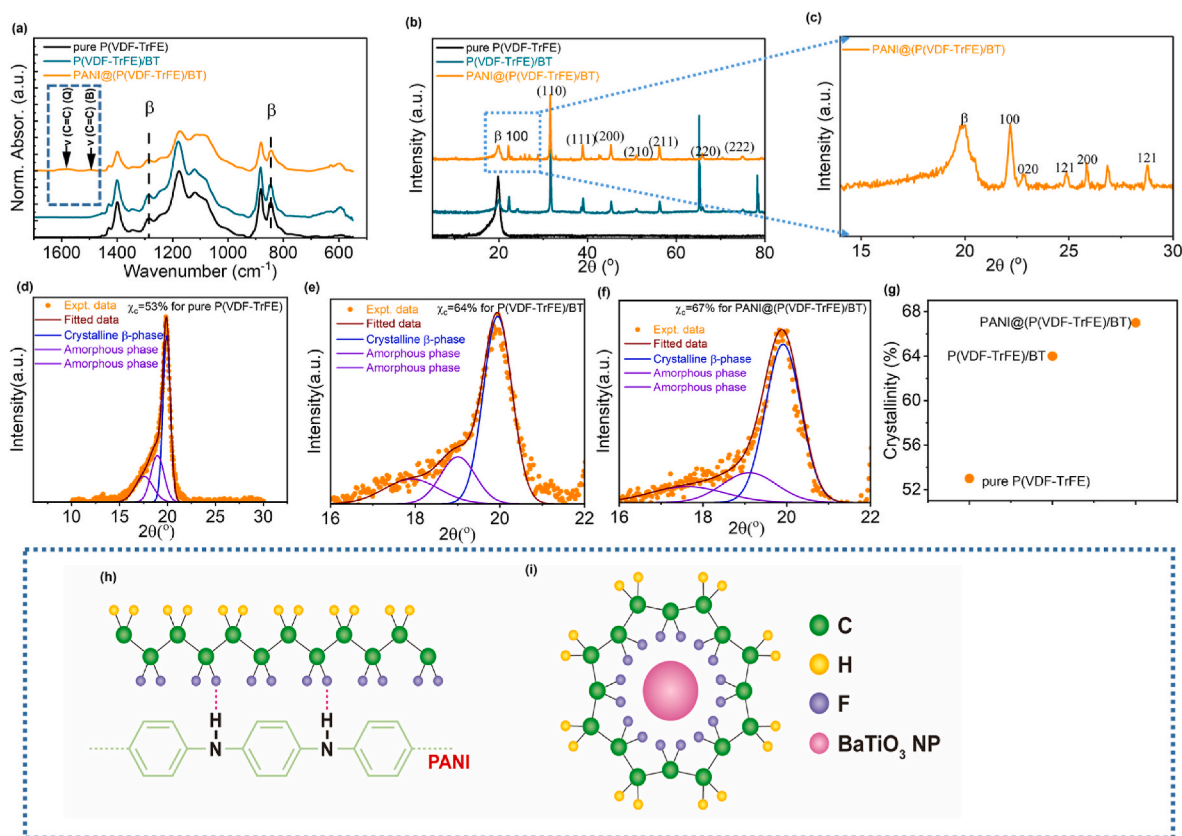


**Fig. 2.** (a) FT-IR spectra of pure P(VDF-TrFE) nanofibers, P(VDF-TrFE)/BT nanocomposite nanofibers, and PANI@P(VDF-TrFE)/BT nanocomposite nanofibers and (b) XRD pattern of pure P(VDF-TrFE) nanofibers, P(VDF-TrFE)/BT nanocomposite nanofibers, and PANI@P(VDF-TrFE)/BT nanocomposite nanofibers, (c) enlarge view of blue marked dotted box of PANI@P(VDF-TrFE)/BT XRD pattern in (b) to visualize additional peaks, nanocomposite nanofibers as pure P(VDF-TrFE) nanofibers. The curve deconvolution of the XRD pattern of (d) pure P(VDF-TrFE) nanocomposite nanofibers, (e) P(VDF-TrFE)/BT nanocomposite nanofibers and (f) PANI@P(VDF-TrFE)/BT nanocomposite nanofibers. (g) Crystallinity (%) comparison of pure P(VDF-TrFE) nanofibers, P(VDF-TrFE)/BT nanocomposite nanofibers, and PANI@P(VDF-TrFE)/BT nanocomposite nanofibers. Illustration of the mechanism of  $\beta$ -phase formation on (h) BT nanoparticles in the P(VDF-TrFE)/BT composite nanofibers and (i) PANI in the PANI@P(VDF-TrFE)/BT nanocomposite nanofibers.

quinoid (Q) and benzenoid (B) ring respectively (Fig. 2a and Fig. S1a) [32,33]. From Fig. S1a, it is obvious that, the quinoid (Q) and benzenoid (B) ring are absent in the pure P(VDF-TrFE) nanofibers and P(VDF-TrFE)/BT nanocomposite nanofibers. Furthermore, the dipolar orientation ( $f_{\text{dipolar}}$ ) of the  $\text{CH}_2/\text{CF}_2$  dipoles within pure P(VDF-TrFE) nanofibers, P(VDF-TrFE)/BT nanocomposite, and PANI@P(VDF-TrFE)/BT nanocomposite nanofibers was evaluated considering the absorption ratio of  $1180\text{ cm}^{-1}$  and  $1285\text{ cm}^{-1}$  peaks in FT-IR spectra (Fig. S1b) [34]. It is noteworthy to mention that the dipolar orientation ( $f_{\text{dipolar}}$ ) of PANI@P(VDF-TrFE)/BT nanocomposite nanofibers is highest in comparison to that of the pure P(VDF-TrFE) nanofibers, P(VDF-TrFE)/BT nanocomposite nanofibers. The  $\beta$ -phase content was calculated using the Beer–Lambert law,  $F_{\beta} = \frac{A_{841}}{\left(\frac{K_{841}}{K_{762}}\right) A_{762} + A_{841}} \times 100\%$ ,

where  $A_{762}$  and  $A_{841}$  represent the absorbances at  $762\text{ cm}^{-1}$  and  $841\text{ cm}^{-1}$  respectively, and  $K_{762} = 6.1 \times 10^4\text{ cm}^2\text{ mol}^{-1}$  and  $K_{841} = 7.7 \times 10^4\text{ cm}^2\text{ mol}^{-1}$  denote the absorbance coefficient corresponding to wave numbers [10]. After PANI coating, the P(VDF-TrFE)/BT nanocomposite nanofibers with 10-wt% BT NPs showed the highest  $\beta$ -phase content ( $F_{\beta} \approx 92\%$ ), while the P(VDF-TrFE)/BT composite nanofiber showed the maximum  $\beta$ -phase content ( $F_{\beta} \approx 83\%$ ), which was higher than that of pure P(VDF-TrFE) nanofibers ( $F_{\beta} \approx 75\%$ ).

The XRD analysis (Fig. 2b) results were consistent with the FT-IR spectra. The XRD analyses (Fig. 2b) showed that the pure P(VDF-TrFE), P(VDF-TrFE)/BT, and PANI@P(VDF-TrFE)/BT nanocomposite nanofibers exhibited a diffraction pattern at  $19.9^\circ$ , which corresponded to the sum of the (110) and (200) reflections of the  $\beta$ -polar phase [10,

35]. The nanocomposite nanofibers showed additional diffraction patterns at  $2\theta = 22.1^\circ, 29.4^\circ, 32.5^\circ, 45.4^\circ, 48.1^\circ, 56.0^\circ, 62.7^\circ$ , and  $69.2^\circ$ , which corresponded to the (100), (110), (111), (200), (210), (211), (220), and (222) crystallographic planes of the tetragonal phase of BT as confirmed by comparing the observed pattern with the JCPDS (# 073644) ICDD pattern; this indicated that the BT NPs were successfully incorporated into the P(VDF-TrFE) nanofibers. The XRD of the PANI@P(VDF-TrFE)/BT composite nanofibers also showed the presence of the characteristic peaks of BT NPs, but with a slight shift to the lower angles [36]. This shift is might be due to the chemical interaction between the PANI and BT NPs. It is a clear evidence of some additional peaks present in the XRD pattern of PANI@P(VDF-TrFE)/BT composite nanofibers (Fig. 2b). The enlarge view of the XRD pattern of PANI@P(VDF-TrFE)/BT composite nanofibers exhibits some other crystalline peaks at  $22.1^\circ, 22.7^\circ, 25.8^\circ$ , and  $28.7^\circ$  correspond to (020), (121), (200), and (121) reflections arising from PANI (Fig. 2c) [32].

By applying the deconvolution method, the degree of crystallinity ( $\chi_c$ ) of the pure and nanocomposite nanofibers with and without PANI coating were calculated from the equation  $\chi_c = \frac{\sum A_{cr}}{\sum A_{cr} + \sum A_{amr}} \times 100\%$ , where  $\sum A_{cr}$  and  $\sum A_{amr}$  are the summation of integral area of the crystalline peaks and amorphous halo, respectively [10]. The overall crystallinity of the PANI@P(VDF-TrFE)/BT nanocomposite nanofibers was higher ( $\chi_c \approx 67\%$ ) than those of the P(VDF-TrFE)/BT nanocomposite nanofibers ( $\chi_c \approx 64\%$ ) and pure P(VDF-TrFE) nanofibers ( $\chi_c \approx 53\%$ ) (Fig. 2d–f). The comparison of degree of crystallinity ( $\chi_c$ ) of the pure and nanocomposite nanofibers with and without PANI coating is

shown in Fig. 2g. The improvement stems primarily from the interfacial interaction of the BT NPs and PANI surface charges with the  $-\text{CH}_2/-\text{CF}_2$  groups of the P(VDF-TrFE) chain. In the case of BT NPs, during electrospinning, the ferroelectric domains of the BT NPs are aligned in the presence of an electric field, leading to increase polarization at the interface of the BT NPs and the P(VDF-TrFE) chain, which increases the piezoelectricity of the nanocomposite nanofibers [37]. By contrast, PANI-coated P(VDF-TrFE)/BT nanocomposite nanofibers enhance the space charge conduction owing to the high charge-carrier mobility of the conducting PANI leading to more electron flow within the PENG. It was observed experimentally that PANI@P(VDF-TrFE)/BT nanocomposite nanofibers possess higher conductivity than P(VDF-TrFE)/BT nanocomposite nanofibers (explained later). Thus, PANI@P(VDF-TrFE)/BT nanocomposite nanofibers exhibited improved piezoelectric properties. The schematic diagram of the proposed interfacial interaction between P(VDF-TrFE) chains and BT NPs as well as PANI is presented in Fig. 2h and i. PANI promotes  $\beta$ -phase formation because of the steric dipole–dipole interactions between the  $-\text{CF}_2$  groups of PVDF and the  $(=\text{N}-\text{H})^+$  groups of PANI, which favors the *trans*-conformation of the highly polar  $\beta$ -phase (Fig. 2h). Furthermore, the interfacial interaction of BT NPs with the  $-\text{CH}_2/-\text{CF}_2$  groups of the P(VDF-TrFE) chain (Fig. 2i) improves the polar  $\beta$ -phase in the nanocomposite nanofiber. This organized arrangement of dipoles promotes a higher polarization in the crystalline lattice, resulting in improved piezoelectric properties.

The FE-SEM images of the as-prepared pure P(VDF-TrFE) nanofibers and 10-wt% BT NP-embedded P(VDF-TrFE)/BT nanocomposite nanofibers revealed a smooth surface and uniform thickness without any bead defects, whereas the PANI@P(VDF-TrFE)/BT nanocomposite nanofibers were characterized by a nanofibrous and coarse surface (Fig. 3a–c). Clearly, PANI was uniformly coated on the P(VDF-TrFE)/BT nanocomposite nanofibers (Fig. 3a). The average diameter of the as-prepared nanofibers was calculated using ImageJ software, considering the diameters of 20 individual nanofibers. The mean diameter for the pure P(VDF-TrFE), P(VDF-TrFE)/BT, and PANI@P(VDF-TrFE)/BT nanocomposite nanofibers was found to be 650, 505, and 551 nm, respectively (Fig. 3a and S2a–d). A reduction in the diameter of the P(VDF-TrFE)/BT nanocomposite nanofibers compared to pure P(VDF-

TrFE) fiber is attributed to the increased total charge originating from the BT NPs within the electrospinning the P(VDF-TrFE)/BT solution enhancing the exerted force in the electrospinning jet and reducing the fiber diameter [38]. It is important to note that the increase of PANI@P(VDF-TrFE)/BT fiber diameter ( $\sim 551$  nm) was due to the PANI coating to the P(VDF-TrFE)/BT fiber ( $\sim 505$  nm) which was conducted after electrospinning through immersing the P(VDF-TrFE)/BT fiber into PANI polymerization solution (details are provided in experimental section 4.3).

The EDS and corresponding elemental mapping confirmed the presence and uniform distribution of elemental carbon, oxygen, fluorine, barium, titanium, and nitrogen in the PANI@P(VDF-TrFE)/BT nanocomposite nanofibers (Fig. 3a–c). The presence of nitrogen in weight percentage of the elemental composition confirmed the successful PANI coating on P(VDF-TrFE)/BT nanocomposite nanofibers (Fig. 3c). It is important to note that some additional peaks are available in the EDX spectra (Fig. 3c), due to Pt (nanofibers are subjected to Platinum sputtering before FE-SEM analysis), Al (Al foil was used to collect the nanofiber sheet during electrospinning) and specimen room holder etc. [39].

## 2.2. Energy-harvesting performance and figure-of-merit improvement

To investigate the material functionality for enhancing the mechanical energy-harvesting performances, systematic studies were conducted by fabricating nanofibers based piezoelectric nanogenerators for four different wt% (6, 10, 14, and 18 wt%) of BT NPs incorporated P(VDF-TrFE) composite nanofibers. On increasing concentration of BT NPs in the range of 6–18 wt% (Figs. S3a and b) the generated  $V_{oc}$  (Fig. S3a) and  $I_{sc}$  (Fig. S3b) were increased and reached a maximum value of 29.6 V and 1.9  $\mu\text{A}$  respectively with the BT NPs concentration of 10 wt% and beyond this concentration, the  $V_{oc}$  and  $I_{sc}$  were decreased. This phenomenon can be attributed to the agglomeration of BT NPs within nanofibers can have a significant impact on the properties and performance of the composite material being produced, including reduced interfacial interactions, dopants sedimentation in electrospinning tubes, resulting decreased  $\beta$ -phase content, and a lower degree of crystallinity [40]. The optimized PENG with 10 wt% BT NPs

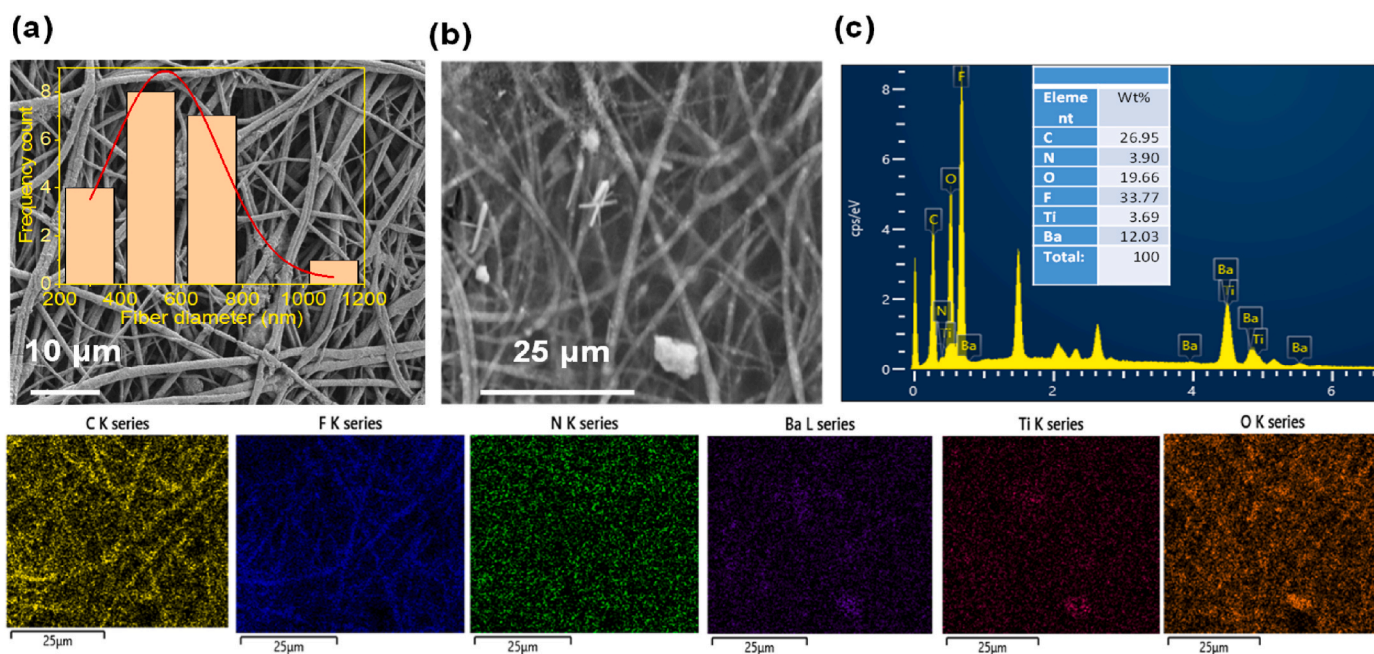


Fig. 3. (a) FE-SEM images with fiber diameter distribution (right upper inset), (b) FE-SEM images for which (c) EDS and elemental mapping was performed on PANI@P(VDF-TrFE)/BT nanocomposite nanofibers.

incorporated P(VDF-TrFE) (i.e., P(VDF-TrFE)/BT) exhibited highest performance in comparison to other wt%. Henceforth, this 10 wt% BT NPs incorporated P(VDF-TrFE) (i.e., P(VDF-TrFE)/BT) is chosen for PANI coating as explained in the experimental section. The open-circuit output voltage ( $V_{oc}$ ) and short-circuit current ( $I_{sc}$ ) of the pure P(VDF-TrFE) nanofibers was found to be 10 V and 0.6  $\mu$ A, respectively, under an iterative pressure of 83.4 kPa (Fig. 4a and b). The optimized P(VDF-TrFE)/BT nanocomposite nanofiber-based PENG generated a  $V_{oc}$  of  $\sim$ 29.6 V and  $I_{sc}$  of  $\sim$ 1.9  $\mu$ A (Fig. 4a and b). The reason for the higher electrical output is the ferroelectric property of the BT NPs, because of which the P(VDF-TrFE)/BT nanofibers possess higher  $\beta$ -phase content, degree of crystallinity, and longitudinal piezoelectric coefficient ( $d_{33}$ ) (discussed later) compared to the pure P(VDF-TrFE) nanofibers. The performance of the P(VDF-TrFE)/BT nanocomposite nanofiber-based PENG was further improved by PANI coating on the P(VDF-TrFE)/BT nanocomposite nanofibers. The PA-PENG generated a  $V_{oc}$  of  $\sim$ 68 V and  $I_{sc}$  of  $\sim$ 3  $\mu$ A, which were respectively 2.2 and 1.5 times higher than those of the P(VDF-TrFE)/BT nanocomposite nanofiber-based PENG. This improvement is attributed to the successful coating of this conductive polymer with PANI, through which the P(VDF-TrFE)/BT nanocomposite nanofibers are expected to exhibit a significant improvement in conductivity, showing an enhancement in current. Experimentally, we observed that the PANI@P(VDF-TrFE)/BT nanocomposite nanofiber possessed higher conductivity than that of the pure P(VDF-TrFE), P(VDF-TrFE)/BT, and PANI@P(VDF-TrFE) nanocomposite nanofiber (Fig. 4c). The linear relationship between the current and voltage for the PANI@P(VDF-TrFE)/BT, PANI@P(VDF-TrFE), P(VDF-TrFE)/BT, and pure P(VDF-TrFE) nanocomposite nanofibers is shown in Fig. 4c. The volume resistivity of the nanocomposite nanofibers was estimated from the equation  $\rho_v = R_v \frac{A}{t}$ , where A and t are the electrode area and thickness of the nanocomposite nanofibers, respectively, and  $R_v$  is the inverse of the slope of the current-voltage (I-V) plot. The estimated volume resistivities of the pure P(VDF-TrFE), P(VDF-TrFE)/BT, PANI@P(VDF-TrFE), and PANI@P(VDF-TrFE)/BT nanocomposite nanofibers were  $0.036 \times 10^{13}$ ,  $0.025 \times 10^{13}$ ,  $0.022 \times 10^{13}$ , and  $0.02 \times 10^{13} \Omega \text{ cm}$ , respectively. Accordingly, the volume conductivities (inverse of resistivity) for the pure P(VDF-TrFE), P(VDF-TrFE)/BT, PANI@P(VDF-TrFE), and PANI@P(VDF-TrFE)/BT nanocomposite nanofibers were  $27.4 \times 10^{-13}$ ,  $40 \times 10^{-13}$ ,  $45.45 \times 10^{-13}$ , and  $50 \times 10^{-13} \text{ S cm}^{-1}$ , respectively. The synergistic effect between the BT NPs in P(VDF-TrFE) and PANI coating in P(VDF-TrFE)/BT nanocomposite nanofibers improved the open-circuit voltage and current simultaneously. The  $d_{33}$  values of the nanofibers were calculated with the quasistatic method using the equation  $d_{33} = Q_e/F$  where,  $Q_e = \int I_{sc} dt$  represents the charge generated under an impact force (F) of 33.4 N. The highest piezoelectric coefficient ( $d_{33}$ ) values of  $\sim$ 62 and  $\sim$ 53  $\text{pC N}^{-1}$  for PANI @P(VDF-TrFE)/BT and P(VDF-TrFE)/BT, respectively, were observed, which were higher than those of pure P(VDF-TrFE) ( $\sim$ 36  $\text{pC N}^{-1}$ ) and previously developed P(VDF-TrFE) composite nanofibers (Tables S1 and S2). Further, to analyze the performance of the device, the piezoelectric figure of merit ( $FoM \approx g_{33} \cdot d_{33}$ ) was estimated for the pure P(VDF-TrFE) nanofiber-, P(VDF-TrFE)/BT-, and PANI@P(VDF-TrFE)/BT nanocomposite nanofiber-based PENGs [10]. The estimated piezoelectric voltage coefficient was found as,  $g_{33} \approx \frac{V_{oc}}{\sigma_a \times t} = 2.32 \text{ V m N}^{-1}$ , where  $\sigma_a = 83.4 \text{ kPa}$  is the stress magnitude and t is the thickness of PA-PENG. Thus, the PANI@P(VDF-TrFE)/BT nanocomposite nanofiber-based PENG exhibited a superior piezoelectric figure of merit ( $FoM \approx g_{33} \cdot d_{33} \approx 14.4 \times 10^{-11} \text{ Pa}^{-1}$ ) compared to the P(VDF-TrFE)/BT nanocomposite nanofiber-based ( $g_{33} \sim 1.01 \text{ V m N}^{-1}$ , and  $FoM \sim 5.4 \times 10^{-11} \text{ Pa}^{-1}$ ) and pure P(VDF-TrFE) nanofiber-based PENGs ( $g_{33} \sim 0.34 \text{ V m N}^{-1}$  and  $FoM \sim 1.2 \times 10^{-11} \text{ Pa}^{-1}$ ) as well as other various recently reported PENGs (Fig. 4d) [10,11,41–45].

### 2.3. Sensitivity and power output performance

The rectified output voltage of the PA-PENG was 66 V (Fig. 4e). Further, the sensitivity performance of the PA-PENG was assessed by conducting a series of tests under varying applied-pressure amplitudes ( $\sigma_a$ ) ranging from 33 to 85.8 kPa (Fig. 4f). The  $V_{oc}$  of the PA-PENG exhibited an increasing trend with an increase in  $\sigma_a$ . However, a marginal increase in  $V_{oc}$  was observed upon the application of an impact pressure amplitude of 83.4 kPa, which aligns with the principles of piezoelectric theory [46]. The developed output voltage varied almost linearly with the increase in applied stress amplitude in the medium-pressure regime, which is consistent with the piezoelectric theory as seen in Fig. 4g. The  $V_{oc}$  of the PA-PENG demonstrated a proportional increase in the medium-pressure regime but experienced a slight decrease at a pressure of 85.8 kPa. This phenomenon can be attributed to the theoretical limits of effective strain in piezoelectric materials when they are subjected to high pressures [47–49]. At elevated pressure levels, the piezoelectric materials may approach their strain limits, which results in reduced charge generation and subsequently causes a slight decrease in  $V_{oc}$  (Fig. 4f). This observation highlights the importance of optimizing pressure levels to maximize the energy-harvesting performance of PENGs. Next, the mechano-sensitivity ( $S_M$ ) was calculated to quantify the dynamic mechanical stimulus-sensing ability of the PA-PENG.  $S_M$  is defined as the ratio of change in  $V_{oc}$  to the change in applied pressure amplitude [10]. The  $S_M$  of the PA-PENG was determined to be  $\sim$ 1.2  $\text{V kPa}^{-1}$  in the medium-pressure (10–100 kPa) regime (Fig. 4g). Furthermore, the  $S_M$  values of the PA-PENG are higher than those of recently reported PENGs (Fig. 4h) [10,50–55]. The superior mechano-sensitivity and wide-range pressure detection exhibited by the PA-PENG make it a potential candidate for high-performance energy-harvesting and sensing applications, particularly in wearable devices engineered to capture and convert biomechanical energy produced by human body movements such as running, jumping, and walking.

The instantaneous voltage drop ( $V_L$ ) and power density (P) of all the PA-PENGs were measured under a constant applied pressure ( $\sigma_a \approx 83.4 \text{ kPa}$ ) while varying the external load resistance ( $R_L$ ) (Fig. 4i). The power density of the PA-PENG was estimated using the formula  $P = \frac{V_L^2}{A \cdot R_L}$ , where A is the effective surface area and  $V_L$  is the voltage drop across the load resistance  $R_L$ . The estimated maximum power density and corresponding load resistance were  $225 \text{ mW m}^{-2}$  and  $R_L \approx 10 \text{ M}\Omega$ , respectively. This indicates that the device is capable of driving a load resistance in the order of  $10 \text{ M}\Omega$ . The generated power density of the proposed PA-PENG is higher than that of the reported nanofibers-based PENGs (Table S1). The superior instantaneous power density of the PA-PENG was sufficient to turn on more than 20 commercial light-emitting diodes (LEDs) without the need for any external storage system (Video S1).

To demonstrate the potential application of the PA-PENG in energy storage and rapid charging systems, the device was connected to three commercial capacitors with capacitances of 1.0, 4.7, and  $10 \mu\text{F}$  individually through a full-wave bridge rectifier circuit (Fig. 4j). Each of the three capacitors was charged individually to their respective saturation voltages of 4.3, 3.7, and 3.4 V within 105, 109, and 210 s, respectively. The  $\tau$  values for all the capacitors were calculated to assess the charging rate and energy supply ability of the PA-PENG (right lower inset, Fig. 4j). The energy (W) stored in the capacitors was  $\sim$ 9.2,  $\sim$ 32, and  $\sim$ 57.8  $\mu\text{J}$ , estimated from formula  $W = \frac{CV_s^2}{2}$ , where C is the capacitance of the charging capacitor and  $V_s$  is the saturation voltage. The performance of the PA-PENG under different finger-tapping conditions was characterized, and a maximum generated  $V_{oc}$  of  $\sim$ 40 V was achieved under three-finger pressure (Fig. 4k). To evaluate the long-term stability of the PA-PENG, cyclic fatigue testing was conducted by applying human hand-induced uniaxial compressive stress with an amplitude of  $\sim$ 83.4 kPa over several months (Fig. 4l).

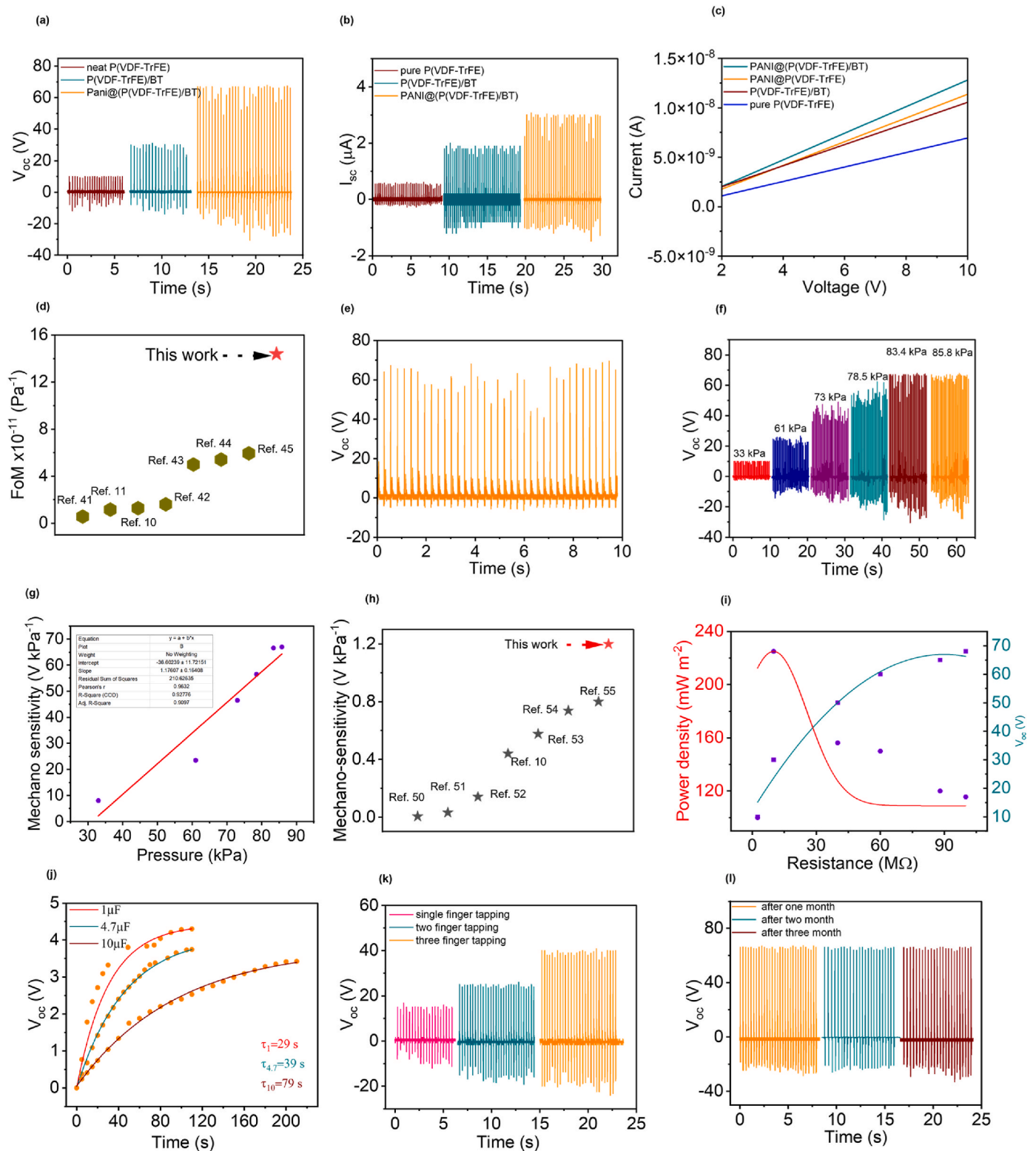


**Fig. 4.** Piezoelectric performance of nanogenerators. (a) Open-circuit output voltage ( $V_{oc}$ ) and (b) short-circuit current ( $I_{sc}$ ) for pure P(VDF-TrFE) nanofibers, P(VDF-TrFE)/BT nanocomposite nanofiber-, and PANI@P(VDF-TrFE)/BT (PA-PENG) nanocomposite nanofiber-based PENGs. (c) I-V characteristics of the PANI@P(VDF-TrFE)/BT, PANI@P(VDF-TrFE), P(VDF-TrFE)/BT, and pure P(VDF-TrFE) nanocomposite nanofibers, (d) comparison of figure of merit of the PA-PENG with recently reported works, and (e) rectified output voltage of the PA-PENG. Sensitivity and output performance of the PA-PENG. (f) Pressure-dependent open-circuit output voltage ( $V_{oc}$ ) of the PA-PENG, (g) mechano-sensitivity plot of the PA-PENG, (h) comparison of mechano-sensitivity of the PA-PENG with reported PENGs, (i) variation in the output voltage and power density of the PA-PENG with external load resistances, (j) capacitor-charging performance of the PA-PENG for different capacitor values, (k) open-circuit output voltage ( $V_{oc}$ ) under different finger-tapping conditions (one, two, and three fingers), and (l) long-term stability testing of the PA-PENG under constant mechanical stress.

## 2.4. Self-powered wearable sensor application in human motion detection

The demand for self-powered wearable sensors is continuously increasing owing to its application in the early detection of diseases and continuous monitoring of health through the recording of different vital signs, including bending of different muscles and joints from different body parts because of activities such as running and jumping. For evaluating the real-time application of the PA-PENG as a self-powered wearable sensor in different parts of the human body for measuring human physiological signals, the PA-PENG was adhered to different parts of the body (arm, knee, wrist, finger, and sole) to record data as illustrated in Fig. 5a–f. The generated voltage waveforms were inspected at these locations and revealed unique responses in terms of signal duration and waveform pattern intensity. For example, the voltage generated by running was 2.5 V (Fig. 5a), where the peaks were followed by an oscillation of 2.8 Hz, which is very close to the resonant step frequency (2.6–2.8 Hz) of a running human [56]. Moreover, the voltage harvested from jumping had a peak of ~5 V with the lowest oscillation owing to prolonged time spans of jumping motion (Fig. 5b). These results suggest that this device could be utilized in smart shoes for gait recognition and walking speed analysis while maintaining high stability under continuous stress. The PA-PENG was attached to fingers, and a voltage output waveform of 2 V was generated under the bending and release condition (Fig. 5c). Fig. 5d displays the output voltage responses to the arm muscle movement, which indicates the arm muscle twitches and spasms. Furthermore, the wearable sensor was attached to the knee joint to monitor joint and leg muscle motion during patellar reflex. Fig. 5e depicts the negative and positive pulses as the knee bends and releases. Finally, the sensor was attached to the wrist joint; the response corresponding to wrist joint movement is shown in Fig. 5f. All the above results verified the feasibility of the PA-PENG device as a self-powered wearable sensor for human motion monitoring, detection, and

recognition, revealing its potential for exercise tracking and rehabilitation.

## 3. Conclusions

In summary, we successfully polymerized aniline on P(VDF-TrFE)/BT nanocomposite nanofibers in a very simple, facile, and cost-effective way. The ferroelectric BT NPs improved the piezoelectric coefficient up to  $62 \text{ pC N}^{-1}$ , while PANI reduced the internal impedance of the nanocomposite and consequently that of the overall device, which collectively improved the  $V_{oc}$  to ~68 V,  $I_{sc}$  to ~3  $\mu\text{A}$ , power density of  $225 \text{ mW m}^{-2}$ , and piezoelectric figure of merit ( $FoM \sim 14.4 \times 10^{-11} \text{ Pa}^{-1}$ ) compared to those of the P(VDF-TrFE)/BT nanocomposite nanofiber-based ( $FoM \sim 5.4 \times 10^{-11} \text{ Pa}^{-1}$ ) and pure P(VDF-TrFE) nanofiber-based ( $FoM \sim 1.2 \times 10^{-11} \text{ Pa}^{-1}$ ) PENGs as well as various other state-of-the-art PVDF-based nanofibers. The PA-PENG could drive more than 10 commercial LEDs and charge three different commercial capacitors directly to realize a self-powered energy-harvesting system. In addition, the excellent mechano-sensitivity ( $1.2 \text{ V kPa}^{-1}$ ) of the device indicates its promising potential application in self-powered wearable sensors for capturing various human motions, including gestures and finger motion, which paves the way for futuristic robotics-based applications.

## 4. Experimental section

### 4.1. Materials

Poly(vinylidene fluoride-co-trifluoroethylene) (P(VDF-TrFE)) (68/32) powder, barium titanate ( $\text{BaTiO}_3$ ) (BT) powder (diameter  $\leq 100 \text{ nm}$ ), butan-2-one, aniline ( $\text{C}_6\text{H}_5\text{NH}_2$ ), perchloric acid ( $\text{HClO}_4$ ), and ammonium persulfate were purchased from Sigma-Aldrich Korea Co.,

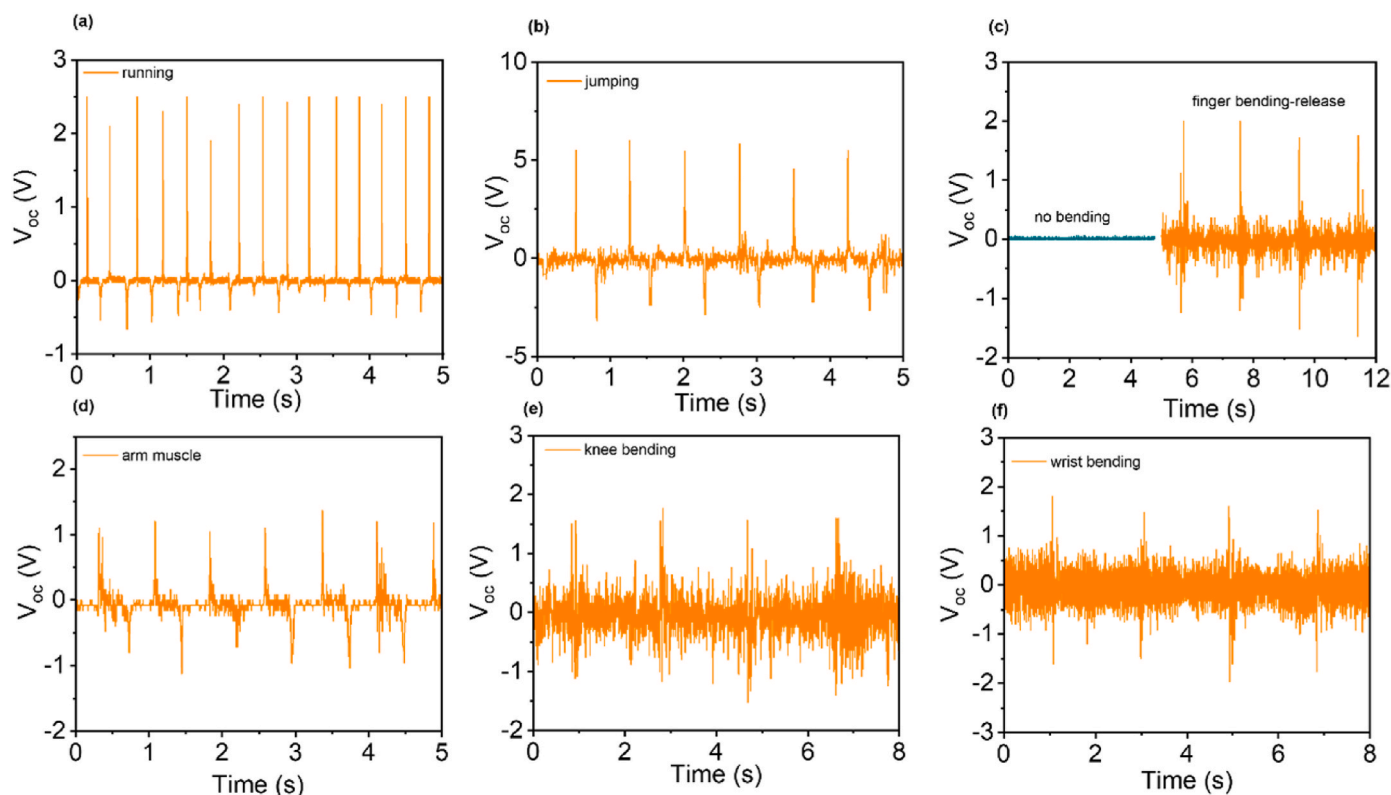


**Fig. 5.** Real-time application of the PA-PENG as a self-powered wearable sensor in different parts of the human body for measuring biomedical activity. Output voltage generation from the PA-PENG used to monitor different human activities: (a) running, (b) jumping, (c) finger bending and release, (d) arm muscle movement, (e) knee joint motion, and (f) wrist bending.

Ltd., South Korea, and Ni–Cu-coated polyester microfabric electrodes were purchased from Solueta Co. Ltd., South Korea. All the chemicals were of analytical reagent grade and used without any further purification.

#### 4.2. Preparation of pure P(VDF-TrFE) nanofibers and composite nanofibers

First, the spinning solutions were prepared by dissolving 12-wt% P(VDF-TrFE) in butan-2-one solvent, followed by stirring for 4 h at 60 °C. BT NPs at 10 wt% were mixed into the above solution, which was then sonicated for 60 min at room temperature to ensure the homogeneous dispersion of BT NPs in the P(VDF-TrFE) matrix. Next, the resulting solution was vigorously stirred for 4 h at 700 rpm at 60 °C and subsequently sonicated for 10 min at room temperature. The electrospinning solution was taken in a 10-mL hypertonic syringe with a diameter of 0.8 mm to initiate the electrospinning process. The solution was dispensed through a syringe pump and injected into the needle at a flow rate of 1.2 mL h<sup>-1</sup>. The nanofibers were deposited on an aluminum foil wrapped over a rotating drum collector at a rotation speed of 100 rpm, and a tip-to-collector distance of 10 cm was maintained. The applied DC voltage between the needle tip and the rotating drum collector was ~15 kV. Additionally, for systematic study, the BT NPs were added into 12 wt% pure P(VDF-TrFE) solutions with varying weight ratios (6, 14, and 18 wt%) and all the composite nanofibers were fabricated. We referred all the composite nanofibers as P(VDF-TrFE)/BT-06, P(VDF-TrFE)/BT-10, P(VDF-TrFE)/BT-14, and P(VDF-TrFE)/BT-18 as per 6–18 wt%. The fabricated optimized nanocomposite nanofibers with 10-wt% BT NPs are referred to as P(VDF-TrFE)/BT nanocomposite nanofibers herein. A control solution containing 12-wt% P(VDF-TrFE) without BT NPs was prepared and electrospun under identical conditions to prepare a pure P(VDF-TrFE) nanofiber mat for comparative experiments. The pure P(VDF-TrFE) nanofiber and all the nanocomposite nanofiber samples were dried at 60 °C for 8 h to remove residual solvents and obtain stable nanofibers. The average thickness of the nanofibers mats is approximately 150 ± 30 μm.

#### 4.3. Deposition of PANI on pure P(VDF-TrFE) nanofiber and P(VDF-TrFE)/BT nanocomposite nanofiber samples

First, the optimized 10 wt% BT incorporated P(VDF-TrFE) (P(VDF-TrFE)/BT) nanocomposite nanofibers were cut to a required size from the fabricated whole nanofiber sheet. Meanwhile, a PANI growth or polymerization solution was prepared by mixing 0.8 ml of aniline monomer with 100 ml of 1-M perchloric acid and stirred for 10 min at room temperature (25–30 °C). The resulting solution was then mixed with 2.5 ml of 0.1-M ammonium persulfate and stirred for 2 min to initiate the polymerization of aniline. The P(VDF-TrFE)/BT nanocomposite nanofiber sheet cut previously was immersed into the abovementioned solution and left to rest for 24 h for polymerization or to grow PANI on P(VDF-TrFE)/BT nanocomposite nanofibers at 0 °C. Thereafter, the P(VDF-TrFE)/BT nanocomposite nanofiber sheet was removed from the solution, washed with deionized water, and dried at 60 °C. Furthermore, the PANI coated pure P(VDF-TrFE) nanofiber was also prepared following the same procedure as in P(VDF-TrFE)/BT nanocomposite nanofibers. The PANI coated pure P(VDF-TrFE) nanofibers and P(VDF-TrFE)/BT nanocomposite nanofibers were referred to as PANI@P(VDF-TrFE), and PANI@P(VDF-TrFE)/BT nanofibers.

#### 4.4. Fabrication of PA-PENG

The device fabrication process is schematically represented in Fig. 1. The as-prepared nanofiber mats were cut according to the desired dimensions (2.1 cm × 2.1 cm) and utilized as the active layer. These mats were then sandwiched between Cu–Ni polyester microfabric electrodes measuring 2 cm × 2 cm to prevent electrical short circuits or charge

leakage. Copper wires were connected to the top and bottom electrodes for external circuit integration. Finally, the entire assembly was encased in PET adhesive tape to maintain the integrity of the composite nanofibers mats and shield them from external temperature fluctuations and humidity. The total thickness (t) of the as-prepared device was 350 μm. An optical image of the fabricated PA-PENG is shown in Fig. S4a, and the flexibility with different orientations is shown in Figs. S4b–d.

#### 4.5. Characterization

The surface morphology and elemental composition of the as-prepared electrospun nanofibers were investigated using field emission scanning electron microscopy (FE-SEM, JEOL, JSF7900F) at an acceleration voltage of 2.0 kV and energy-dispersive X-ray spectroscopy (EDS) (Oxford Instruments, Ultim Max) techniques. Before the scanning electron microscopy analysis, the as-prepared electrospun nanofibers were subjected to platinum sputtering with operational parameters of 90 s and a current of 0.1 mA. The X-ray diffraction (XRD) patterns of the electrospun nanofibers were obtained using an X-ray diffractometer (PANalytical, X'Pert Pro) with CuKα irradiation with a 2θ scanning range of 5°–90° and a scanning speed of 8.5° min<sup>-1</sup>. The vibrational bands and crystalline phases of the electrospun nanofibers were measured using Fourier transform infrared (FT-IR) (PIKE Technologies, Spectrum 3 FT-IR). All the measurements were performed under the attenuated total reflection mode with the following measuring parameters: 4 cm<sup>-1</sup> resolution and 20 scans. Finally, the V<sub>oc</sub> and I<sub>sc</sub> responses from all the PENGs under different applied stresses were recorded using a digital oscilloscope (Tektronix TDS 2014B) and low-noise current preamplifier (Stanford research systems, Model no. SR570), respectively. The high-voltage probe (P5100A) has an input impedance of 40 MΩ ± 1 %. Current–voltage (I–V) measurement was performed by using a Keithley source meter (model no. 2400). The estimated hand-imparted compressive force applied on the devices is depicted in detail in Associated discussion S1.

#### CRediT authorship contribution statement

**Biswajit Mahanty:** Conceptualization, Methodology, Investigation, Data curation, Formal analysis, Validation, Writing – original draft. **Sujoy Kumar Ghosh:** Data curation, Formal analysis, Writing – review & editing. **Dong-Weon Lee:** Resources, Funding acquisition, Validation, Supervision, Writing – review & editing.

#### Declaration of competing interest

The authors declare no competing financial interest.

#### Data availability

Data will be made available on request.

#### Acknowledgements

Funding: This work was supported by the National Research Foundation of Korea (NRF) grant funded by the Korean government (MSIT) (No. RS-2022-00165505) and (No. 2020R1A5A8018367).

#### Appendix A. Supplementary data

Supplementary data to this article can be found online at <https://doi.org/10.1016/j.mtnano.2023.100421>.

#### References

- [1] W. Deng, Y. Zhou, A. Libanori, G. Chen, W. Yang, J. Chen, Piezoelectric nanogenerators for personalized healthcare, *Chem. Soc. Rev.* 51 (2022) 3380.

- [2] M. Yao, Y. Cheng, Z. Zhou, M. Liu, Recent progress on the fabrication and applications of flexible ferroelectric devices, *J. Mater. Chem. C* 8 (2020) 14.
- [3] X. Cao, Y. Xiong, J. Sun, X. Zhu, Q. Sun, Z.L. Wang, Piezoelectric nanogenerators derived self-powered sensors for multifunctional applications and artificial intelligence, *Adv. Funct. Mater.* 31 (2021), 2102983.
- [4] H. Li, S. Lim, High-performance piezoelectric nanogenerators featuring embedded organic nanodroplets for self-powered sensors, *J. Mater. Chem. A* 10 (2022), 14894.
- [5] L. Persano, S.K. Ghosh, D. Pisignano, Enhancement and function of the piezoelectric effect in polymer nanofibers, *Acc. Mater. Res.* 3 (2022) 900–912.
- [6] Z.L. Wang, J. Song, Piezoelectric nanogenerators based on zinc oxide nanowire arrays, *Science* 312 (2006) 242–246.
- [7] W. Wu, S. Bai, M. Yuan, Y. Qin, Z.L. Wang, T. Jing, Lead zirconate titanate nanowire textile nanogenerator for wearable energy-harvesting and self-powered devices, *ACS Nano* 6 (2012) 6231–6235.
- [8] C. Dagdeviren, P. Joe, O.L. Tuzman, K.-I. Park, K.J. Lee, Y. Shi, Y. Huang, J. A. Rogers, Recent progress in flexible and stretchable piezoelectric devices for mechanical energy harvesting, sensing and actuation, *Extreme Mech. Lett.* 9 (2016) 269–281.
- [9] B. Mahanty, S.K. Ghosh, S. Garain, D. Mandal, An effective flexible wireless energy harvester/sensor based on porous electret piezoelectric polymer, *Mater. Chem. Phys.* 186 (2017) 327–332.
- [10] B. Mahanty, S.K. Ghosh, S. Jana, K. Roy, S. Sarkar, D. Mandal, All-fiber acousto-electric energy harvester from magnesium salt-modulated PVDF nanofiber, *Sustain. Energy Fuels* 5 (2021) 1003–1013.
- [11] B. Mahanty, S.K. Ghosh, S. Jana, Z. Mallick, S. Sarkar, D. Mandal, ZnO nanoparticle confined stress amplified all-fiber piezoelectric nanogenerator for self-powered healthcare monitoring, *Sustain. Energy Fuels* 5 (2021) 4389–4400.
- [12] Y. Mao, P. Zhao, G. McConohy, H. Yang, Y. Tong, X. Wang, Sponge-like piezoelectric polymer films for scalable and integratable nanogenerators and self-powered electronic systems, *Adv. Energy Mater.* 4 (2014), 1301624.
- [13] N.R. Alluri, A. Chandrasekhar, J.H. Jeong, S.-J. Kim, Enhanced electroactive  $\beta$ -phase of the sonication-process-derived PVDF-activated carbon composite film for efficient energy conversion and a battery-free acceleration sensor, *J. Mater. Chem. C* 5 (2017) 4833–4844.
- [14] H. Jiang, J. Yang, F. Xu, Q. Wang, W. Liu, Q. Chen, C. Wang, X. Zhang, G. Zhu, VDF-content-guided selection of piezoelectric P(VDF-TrFE) films in sensing and energy harvesting applications, *Energy Convers. Manag.* 211 (2020), 112771, <https://doi.org/10.1016/j.enconman.2020.112771>.
- [15] S.P. Bao, G.D. Liang, S.C. Tjong, Effect of mechanical stretching on electrical conductivity and positive temperature coefficient characteristics of poly(vinylidene fluoride)/carbon nanofiber composites prepared by non-solvent precipitation, *Carbon* 49 (2011) 1758–1768.
- [16] V. Sencadas, R. Gregorio, S.L. Mendez,  $\alpha$  to  $\beta$  phase transformation and microstructural changes of PVDF films induced by uniaxial stretch, *J. Macromol. Sci., Part B: Phys.* 48 (2009) 514–525.
- [17] Y. Huang, G. Rui, Q. Li, E. Allahyarov, R. Li, M. Fukuto, G.-J. Zhong, J.-Z. Xu, Z.-M. Li, P.L. Taylor, L. Zhu, Enhanced piezoelectricity from highly polarizable oriented amorphous fractions in biaxially oriented poly(vinylidene fluoride) with pure  $\beta$  crystals, *Nat. Commun.* 12 (2021) 675.
- [18] J. Kim, J.H. Lee, H. Ryu, J.-H. Lee, U. Khan, H. Kim, S.S. Kwak, S.-W. Kim, High-performance piezoelectric, pyroelectric, and triboelectric nanogenerators based on P(VDF-TrFE) with controlled crystallinity and dipole alignment, *Adv. Funct. Mater.* 27 (2017), 1700702.
- [19] A. Gebrekristos, T.S. Muzata, S.S. Ray, Nanoparticle-enhanced  $\beta$ -phase formation in electroactive PVDF composites: a review of systems for applications in energy harvesting, EMI shielding, and membrane technology, *ACS Appl. Nano Mater.* 5 (2022) 7632–7651.
- [20] S. Ramasundaram, S. Yoon, K.J. Kim, J.S. Lee, Direct preparation of nanoscale thin films of poly(vinylidene fluoride) containing  $\beta$ -crystalline phase by heat-controlled spin coating, *Macromol. Chem. Phys.* 209 (2008) 2516–2526.
- [21] L. Persano, C. Dagdeviren, Y. Su, Y. Zhang, S. Girardo, D. Pisignano, Y. Huang, J. A. Rogers, High performance piezoelectric devices based on aligned arrays of nanofibers of poly(vinylidene fluoride-co-trifluoroethylene), *Nat. Commun.* 4 (2013) 1633.
- [22] Y. Zhang, L. Zhou, X. Gao, C. Liu, H. Chen, H. Zheng, J. Gui, C. Sun, L. Yu, S. Guo, Performance-enhanced flexible piezoelectric nanogenerator via layer-by-layer assembly for self-powered vagal neuromodulation, *Nano Energy* 89 (2021), 106319.
- [23] B. Dudem, A.R. Mule, H.R. Patnam, J.S. Yu, Wearable and durable triboelectric nanogenerators via polyaniline coated cotton textiles as a movement sensor and self-powered system, *Nano Energy* 55 (2019) 305–315.
- [24] R.S. Sabry, A.D. Hussein, PVDF: ZnO/BaTiO<sub>3</sub> as high out-put piezoelectric nanogenerator, *Polym. Test.* 79 (2019), 106001.
- [25] S. Bairagi, S.W. Ali, A hybrid piezoelectric nanogenerator comprising of KNN/ZnO nanorods incorporated PVDF electrospun nanocomposite webs, *Int. J. Energy Res.* 44 (2020) 5545.
- [26] D. Ponnammma, H. Parangusan, A. Tanvir, M.A.A. AlMa'adeed, Smart and robust electrospun fabrics of piezoelectric polymer nanocomposite for self-powering electronic textiles, *Mater. Des.* 184 (2019), 108176.
- [27] M. Hasanazadeh, M.R. Ghahghari, S.M. Bidoki, Enhanced piezoelectric performance of PVDF-based electrospun nanofibers by utilizing in situ synthesized graphene-ZnO nanocomposites, *J. Mater. Sci. Mater. Electron.* 32 (2021), 15789.
- [28] K. Shi, B. Sun, X. Huang, P. Jiang, Synergistic effect of graphene nanosheet and BaTiO<sub>3</sub> nanoparticles on performance enhancement of electrospun PVDF nanofiber mat for flexible piezoelectric nanogenerators, *Nano Energy* 52 (2018) 153.
- [29] J. Gomes, J.S. Nunes, V. Sencadas, S.L. Mendez, Influence of the  $\beta$ -phase content and degree of crystallinity on the piezo- and ferroelectric properties of poly(vinylidene fluoride), *Smart Mater. Struct.* 19 (2010), 065010.
- [30] L. Weng, P. Ju, H. Li, L. Yan, L. Liu, Preparation and characterization of multi shape ZnO/PVDF composite materials, *J. Wuhan Univ. Technol., Mater. Sci.* 32 (2017) 958–962.
- [31] K. Dong, X. Peng, Z.L. Wang, Fiber/fabric-based piezoelectric and triboelectric nanogenerators for flexible/stretchable and wearable electronics and artificial intelligence, *Adv. Mater.* 32 (2020), 1902549.
- [32] K. Maity, S. Garain, K. Henkel, D. Schmeißer, D. Mandal, Self-powered human-health monitoring through aligned PVDF nanofibers interfaced skin-interactive piezoelectric sensor, *ACS Appl. Polym. Mater.* 2 (2020) 862–878.
- [33] M. Sawangphruk, M. Suksomboon, K. Kongsupornsak, J. Khuntilo, P. Srimuk, Y. Sanguansak, P. Klunbud, P. Suktha, P. Chiochan, High-performance supercapacitors based on silver nanoparticle–polyaniline–graphene nanocomposites coated on flexible carbon fiber paper, *J. Mater. Chem. A* 1 (2013) 9630–9636.
- [34] D. Mandal, S. Yoon, K.J. Kim, Origin of piezoelectricity in an electrospun poly(vinylidene fluoride-trifluoroethylene) nanofiber web-based nanogenerator and nano-pressure sensor, *Macromol. Rapid Commun.* 32 (2011) 831–837.
- [35] H. Wei, H. Wang, Y. Xia, D. Cui, Y. Shi, M. Dong, C. Liu, T. Ding, J. Zhang, Y. Ma, N. Wang, Z. Wang, Y. Sun, R. Wei, Z. Guo, An overview of lead-free piezoelectric materials and devices, *J. Mater. Chem. C* 6 (2018) 12446–12467.
- [36] K.F. Qasim, M.A. Mousa, Effect of oxidizer on PANI for producing BaTiO<sub>3</sub>@PANI perovskite composites and their electrical and electrochemical properties, *J. Inorg. Organomet. Polym.* 32 (2022) 3093–3105.
- [37] S.K. Ghosh, J. Kim, M.P. Kim, S. Na, J. Cho, J.J. Kim, H. Ko, Ferroelectricity-coupled 2D-MXene-based hierarchically designed high-performance stretchable triboelectric nanogenerator, *ACS Nano* 16 (2022), 11415.
- [38] D. Mandal, K. Henkel, D. Schmeißer, Improved performance of a polymer nanogenerator based on silver nanoparticles doped electrospun P(VDF-HFP) nanofibers, *Phys. Chem. Chem. Phys.* 16 (2014) 10403–10407.
- [39] Y. Zhuang, J. Li, Q. Hu, S. Han, W. Liu, C. Peng, Z. Li, L. Zhang, X. Wei, Z. Xu, Flexible composites with Ce-doped BaTiO<sub>3</sub>/P (VDF-TrFE) nanofibers for piezoelectric device, *Compos. Sci. Technol.* 200 (2020), 108386.
- [40] J.E. Karbowniczek, D.P. Ura, U. Stachewicz, Nanoparticles distribution and agglomeration analysis in electrospun fiber based composites for desired mechanical performance of poly(3-hydroxybutyrate-co-3-hydroxyvalerate (PHBV) scaffolds with hydroxyapatite (HA) and titanium dioxide (TiO<sub>2</sub>) towards medical applications, *Composites, Part B* 241 (2022), 110011.
- [41] M. Yan, S. Liu, Y. Liu, Z. Xiao, X. Yuan, D. Zhai, K. Zhou, Q. Wang, D. Zhang, C. Bowen, Y. Zhang, Flexible PVDF-TrFE nanocomposites with Ag-decorated BCZT heterostructures for piezoelectric nanogenerator applications, *ACS Appl. Mater. Interfaces* 14 (2022), 53261.
- [42] K. Roy, S. Jana, Z. Mallick, S.K. Ghosh, B. Dutta, S. Sarkar, C. Sinha, D. Mandal, Two-dimensional MOF modulated fiber nanogenerator for effective acoustoelectric conversion and human motion detection, *Langmuir* 37 (2021), 7107–7117.
- [43] S.K. Ghosh, D. Mandal, Synergistically enhanced piezoelectric output in highly aligned 1D polymer nanofibers integrated all-fiber nanogenerator for wearable nano-tactile sensor, *Nano Energy* 53 (2018) 245–257.
- [44] Q. Xu, Z. Wang, J. Zhong, M. Yan, S. Zhao, J. Gong, K. Feng, J. Zhang, K. Zhou, J. Xie, H. Xie, D. Zhang, Y. Zhang, C. Bowen, Construction of flexible piezoceramic array with ultrahigh piezoelectricity via a hierarchical design strategy, *Adv. Funct. Mater.* (2023), 2304402.
- [45] B. Mahanty, S.K. Ghosh, K. Maity, K. Roy, S. Sarkar, D. Mandal, All-fiber pyro- and piezo-electric nanogenerator for IoT based self-powered health-care monitoring, *Mater. Adv.* 2 (2021) 4370.
- [46] D.Y. Park, D.J. Joe, D.H. Kim, H. Park, J.H. Han, C.K. Jeong, H. Park, J.G. Park, B. Joung, K.J. Lee, Self-powered real-time arterial pulse monitoring using ultrathin epidermal piezoelectric sensors, *Adv. Mater.* 29 (2017), 1702308.
- [47] Y. Qi, J. Kim, T.D. Nguyen, B. Lisko, P.K. Purohit, M.C. McAlpine, Enhanced piezoelectricity and stretchability in energy harvesting devices fabricated from buckled PZT ribbons, *Nano Lett.* 11 (2011) 1331–1336.
- [48] X. Feng, B.D. Yang, Y. Liu, Y. Wang, C. Dagdeviren, Z. Liu, A. Carlson, J. Li, Y. Huang, J.A. Rogers, Stretchable ferroelectric nanoribbons with wavy configurations on elastomeric substrates, *ACS Nano* 5 (2011) 3326–3332.
- [49] J. Palosaari, M. Leinonen, J. Hannu, J. Juuti, H. Jantunen, Energy harvesting with a cymbal type piezoelectric transducer from low frequency compression, *J. Electroceram.* 28 (2012) 214.
- [50] S.K. Ghosh, T.K. Sinha, B. Mahanty, D. Mandal, Self-poled efficient flexible “ferroelectric” nanogenerator: a new class of piezoelectric energy harvester, *Energy Technol.* 3 (2015) 1190–1197.
- [51] S.M. Hosseini, A.A. Yousefi, Piezoelectric sensor based on electrospun PVDF-MWCNT-Cloisite 30B hybrid nanocomposites, *Org. Electron.* 50 (2017) 121–129.
- [52] Q.-L. Zhao, G.-P. He, J.-J. Di, W.-L. Song, Z.-L. Hou, P.-P. Tan, D.-W. Wang, M.-S. Cao, Flexible semi-transparent energy harvester with high pressure sensitivity and power density based on laterally aligned PZT single-crystal nanowires, *ACS Appl. Mater. Interfaces* 9 (2017) 24696–24703.
- [53] G. Zhao, X. Zhang, X. Cui, S. Wang, Z. Liu, L. Deng, A. Qi, X. Qiao, L. Li, C. Pan, Y. Zhang, L. Li, Piezoelectric polyacrylonitrile nanofiber film-based dual-function self-powered flexible sensor, *ACS Appl. Mater. Interfaces* 10 (2018) 15855–15863.

- [54] D. Yu, Z. Zheng, J. Liu, H. Xiao, G. Huangfu, Y. Guo, Super flexible and lead-free piezoelectric nanogenerator as a highly sensitive self-powered sensor for human motion monitoring, *Nano-Micro Lett.* 13 (2021) 117.
- [55] S.K. Ghosh, P. Adhikary, S. Jana, A. Biswas, V. Sencadas, S.D. Gupta, B. Tudu, D. Mandal, Electrospun gelatin nanofiber based self-powered bio-e-skin for health care monitoring, *Nano Energy* 36 (2017) 166–175.
- [56] G.A. Cavagna, M. Mantovani, P.A. Willems, G. Musch, The resonant step frequency in human running, *Pflügers Archiv* 434 (1997) 678–684.